ELSEVIER

Contents lists available at ScienceDirect

Ceramics International

journal homepage: www.elsevier.com/locate/ceramint





Complex shape transparent Al₂O₃ fabricated by integrated Spark Plasma Sintering - Additive manufacturing technology

Elisa Torresani a,*, CheolWoo Park , Thomas Grippi , Chris Haines , Eugene A. Olevsky cheolWoo Park , Thomas Grippi , Chris Haines , Eugene A. Olevsky

- ^a San Diego State University, College of Engineering, San Diego, CA, USA
- ^b US Army DEVCOM Army Research Laboratory, Aberdeen Proving Ground, MD, USA
- ^c NanoEngineering, University of California, La Jolla, San Diego, USA

ARTICLE INFO

Handling Editor: Dr P. Vincenzini

Keywords:
Complex shapes
Alumina
Transparent ceramics
Simulation
Spark plasma sintering
Additive manufacturing

ABSTRACT

Spark plasma sintering (SPS) is one of the most promising technologies for producing polycrystalline transparent ceramics. However, it has limitations regarding the complexity of the geometries that can be produced. This study addresses these limitations by combining additive manufacturing techniques with spark plasma sintering. Additionally, a Multiphysics sintering model based on the continuum theory of sintering is employed to predict the outcomes of the SPS process, particularly the microstructure of the densified parts. As a result, the geometrically complex Al_2O_3 transparent parts manufactured in this study exhibit a uniform microstructure, high density (\sim 99 %), and a linear transmittance of 16 % at 490 μ m.

1. Introduction

The need for transparent materials has been growing in many technological areas and applications, such as medical devices, cars, laser lenses, infrared (IR) windows/domes, composite armors, optoelectrical components, and screens for smartphones. Conventional transparent materials (e.g., glasses, polymers) have low mechanical and chemical properties. Some inorganic materials can be optically transparent as single crystals; however, the fabrication or growth of single crystals is a slow and costly process [1–3]. Moreover, obtaining large single crystals of oxide materials with high melting temperatures results in challenges due to the difficulties in controlling the process.

Consequently, the interest in transparent ceramics as substitutes for single-crystal materials has grown in the last decade due to outstanding their advantages such as low cost, large-scale production, and high mechanical and chemical properties [4–6]. Within transparent ceramics, alumina is highly investigated due to its outstanding properties, which make it an interesting material for optical applications in corrosive and hot environments [7].

Conventionally sintered alumina is opaque, since its microstructure is characterized by the presence of elements such as pores, grain boundaries, and structural defects which cause light scattering. Therefore, to achieve optical transparency, one should be able to remove or

limit the concentration and size of such microstructural features.

To attain transparent alumina ceramics, different approaches have been developed to decrease the sources of light scattering. One strategy is to sinter at high temperatures up to 1900 °C for a long time, to promote grain growth and, consequently, reduce the area of grain boundaries. The grain size obtained with this method was around tens of micrometers producing approximately only 10 % of in-line transmittance [8]. The transmittance can be increased up to 15–20 % using a higher sintering temperature which results in grain sizes around hundreds of micrometers but, on the other hand, reduces the mechanical properties. To alleviate this issue, sintering aids are used to improve the transparency attained at lower sintering temperatures with the reduction of the porosity and inhibition of the grain growth [9,10].

A second approach to manufacture transparent Al_2O_3 ceramics consists of the use of pressure-assisted sintering technology such as the Hot Isostatic Pressing (HIP) [11–15]. Using this technology, the in-line transmittance obtained was up to 85 % at 640 nm [15].

More advanced processes to attain transparent ceramics are represented by field-assisted sintering technologies such as Microwave Sintering (MW) and Spark Plasma Sintering (SPS).

In microwave sintering, the consolidation process is activated through a direct and volumetric heating of the material [16–18], which is induced by the adsorption of the microwave energy. Therefore, this

E-mail address: etorresani@sdsu.edu (E. Torresani).

^{*} Corresponding author.

technology, compared with conventional heating, is faster, and capable of reducing the needed temperature for the sintering process [19–23], allowing the improved mechanical properties of the sintered parts. Thanks to these advantages, this technology has been investigated for the production of transparent alumina ceramics [24–27], obtaining in-line transmittance up to 76.5 % at 400 nm [27]. Despite the advantages, MW technology is known for being difficult to control and to obtain consistent results due to the inherent instability problems [28, 29]. In literature, there are some known attempts to improve the stability of the process through the application of pressure to the sample during the process called microwave pressing [30,31].

Spark Plasma Sintering technology allows achieving fast heating (up to 100C°/min) and is largely used to densify alumina with fine grain in a short time. The fast heating, together with the application of pressure, allows even the retention of nano-grains [32-35]. Due to these advantages, SPS has attained great interest for the manufacturing of transparent aluminates [36-44] reaching in-line transmittance of up to 70 % at 645 nm [44]. Despite great capabilities of SPS, this technology is limited to the production of simple shapes, such as cylindrical components. This limitation, which is common for the net shape technologies which involve pressure applications, results in the difficulty to attain a homogeneous microstructure and densification when processing a complex geometry that contains different thicknesses. Sections with large thickness variations result in non-homogeneous densification because the high thickness areas require a larger shrinkage than the overall specimen's volume [45]. In literature, there are different known approaches to overcome this issue, such as multiple punches approaches [46,47], or, in more recent works, the use of a sacrificial material [48] or deformable interfaces [49–51]. These last two approaches have shown their capability to densify complex parts made from different materials and to even obtain internal features such as channels [52].

In the present work, solvent jetting, an additive manufacturing (AM) technology, has been combined with the SPS process, allowing to take advantage of AM and SPS strengths for the production of complex shapes

(AM's strength), and the fast densification of high temperature materials (SPS' strength.) This study addresses the challenges involved in the manufacture of complex transparent alumina parts. Involving a porous sacrificial interface produced using AM, transparent conical parts with 16 % of in-line transmittance at 500 nm were obtained. A comprehensive electro-thermal-mechanical simulation of the process has been conducted to study the complex behavior of the porous assembly during the SPS process.

2. Materials and methods

2.1. Porous sacrificial mold and assembly fabrication

In the present study porous sacrificial molds made by graphite powder have been manufactured using a custom-made solvent jetting printer. In the present work, the mold was designed to obtain a conic transparent part. The printed powder was prepared by mixing in a conventional dry mixer (Turbula®, WAB-Group, Switzerland) for 60 min of the graphite powder (Atlantic Equipment Engineers, 325 mesh) with sugar and maltodextrin. The printing mixture includes up to 75 wt % of graphite, and the remaining 25 wt% contain the mixture of powdered sugar (Wholesome) and maltodextrin (Pure Organic), which were used as binders (12.5 % sugar and 12.5 % maltodextrin). Alumina powder (Sumitomo Chemical, AA-3, single crystals with mean particle size 3.5 μ m) was used as the powder to produce the transparent component. The particle morphology and particle size of each powder are shown in Fig. 1.

The solvent used in the present work was contained in HP 45 Inkjet cartridges and was composed of 8.3%Vol. of Isopropyl alcohol, 8.3%Vol. of diethylene glycol and 83.4%Vol. of DI water. In Fig. 2 the schematic of the different process steps is reported. In the custom-made solvent jetting printer, the preparation layers were spread, then the inkjet cartridge sprayed water-based ink in the designated areas as dictated by the CAD model. This process was repeated layer by layer until the printed

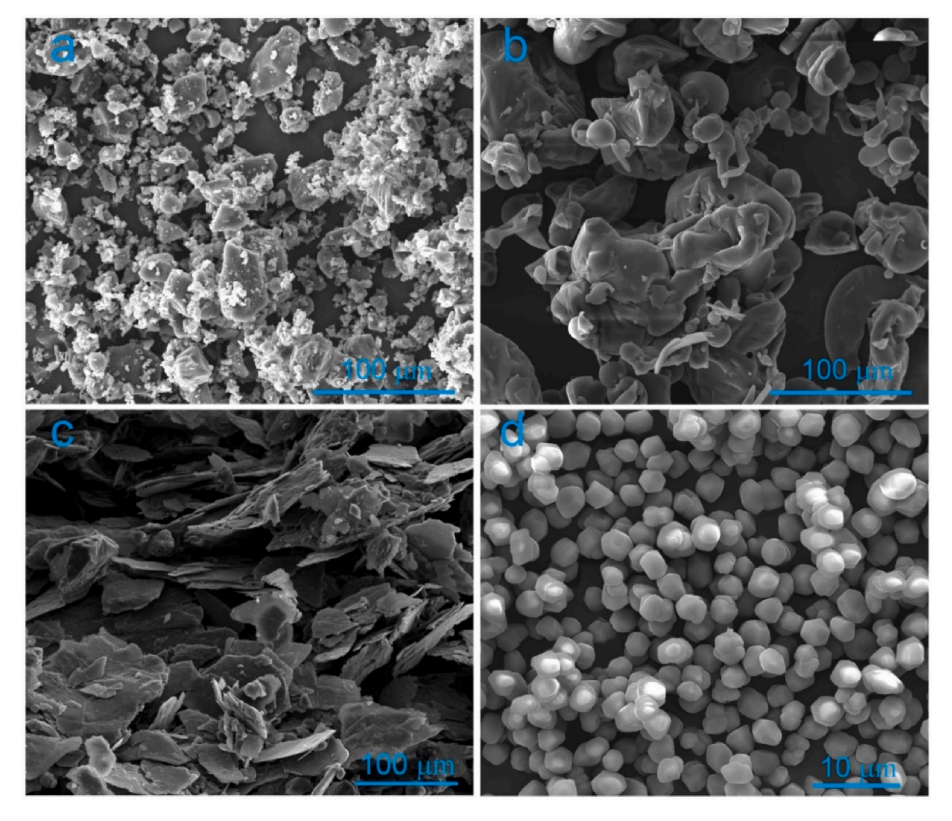


Fig. 1. Powders involved in the present research: a) sugar, b) maltodextrin, c) graphite and d) alumina.

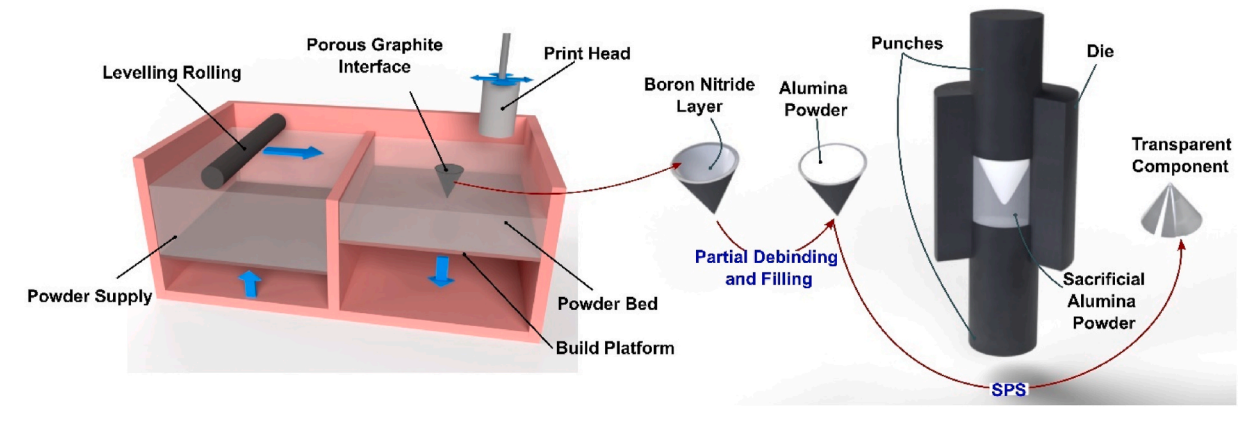


Fig. 2. Schematic of the process, from the manufacturing of the sacrificial mold using solvent jetting to the production of the transparent ceramic cone through the SPS process.

object was completed. Subsequently, the printed samples were cured in a vacuum oven (AccuTemp-0.9, Across International, USA) at 80 °C for 30 min to ensure the samples were dried before using pressurized air to remove loose powder. The mold was subject to partial debinding in vacuum for 1 h at 750 °C to reduce the pollution of the SPS chamber and the contamination of the alumina powder, which could result in decreased transparency prior to sintering. Then, as additional protection against carbon diffusion during the sintering process, a layer of boron nitride was sprayed on the surface of the mold's internal cavity. Once the boron nitride was dried, the mold was filled with a fixed amount of alumina powder. Subsequently, the filled sacrificial mold has been inserted in the graphite die. Since the base diameter of the external surface of the conical interface corresponded to the diameter of the die, it was possible to insert the sacrificial mold in it without causing tilting. Once the interface with the powder was in the die, a graphite foil and punch were inserted to seal the cone's base, and allowing to add a fixed amount of alumina in the surrounding area (sacrificial), obtaining in this way the assembly shown in the schematic presented in Fig. 2.

2.2. Sample consolidation and characterization

The densification was carried out using an SPS device (SPSS Dr. Sinter 515, Fuji Electronics, Japan). An 18 mm diameter graphite die was used as tooling in which the porous assembly was inserted. The assembly has been heated up to $1400\,^{\circ}\mathrm{C}$ with a dwell time of 50 min (Fig. 3); a pressure of $100\,\mathrm{MPa}$ was applied during the entire process. At the end of the dwell time, the sample has been allowed to cool down to ambient temperature naturally. Finally, the assembly has been extracted from the tooling, and the consolidated component has been removed from the sacrificial mold.

Density measurements of all components in the sintering cycle

(alumina powder and graphite mold) were necessary as input parameters for the finite element model described in the following section. The theoretical density of the printed mold was determined using a helium gas pycnometer (Ultrapyc 5000, Anton Paar, Austria). The relative densities of printed porous molds and tap densities of the alumina powder, in both manufactured part and sacrificial area, were then determined via the geometrical measurement method, knowing the amount of powder which was present in the different sections and the volume of the respective area. The bulk densities of the sintered parts were estimated using Archimedes' immersion method following ASTM Standard C373-18. To measure the transparency of the part, the tip of the cone had to be flattened to avoid disturbance of the measurements (Fig. 4).

The transparency in the range of light wavelength between 200 nm and 2500 nm has been measured using UV–Visible analyzer (V-770, Jasco, Japan).

The specimens were sectioned and analyzed using a Scanning Electron Microscopy (FEI Quanta 450, FEI, USA) on polished and etched surfaces, to assess qualitatively and quantitively the material microstructure, with a focus on grain size and porosity. To highlight the grains, the samples were thermally etched at $1000\,^{\circ}\mathrm{C}$ for 20 min.

The hardness in the different samples' locations was measured using a Vickers microhardness tester (402MVD, Wilson Instruments, USA) applying 1 kgf (\sim 9.81 N) load for 10 s.

3. Model

In the present work, a Multiphysics model incorporated in COM-SOLTM finite element software has been involved in predicting the behavior of the porous assembly during the SPS process.

The model framework developed couples the electrical, thermal,

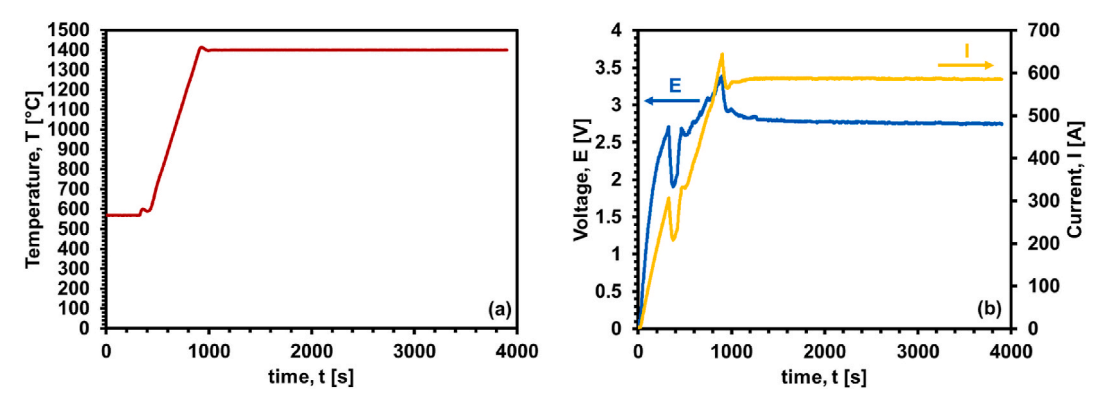


Fig. 3. Experimental data of the SPS process (a) Temperature, (b) Voltage and Current.

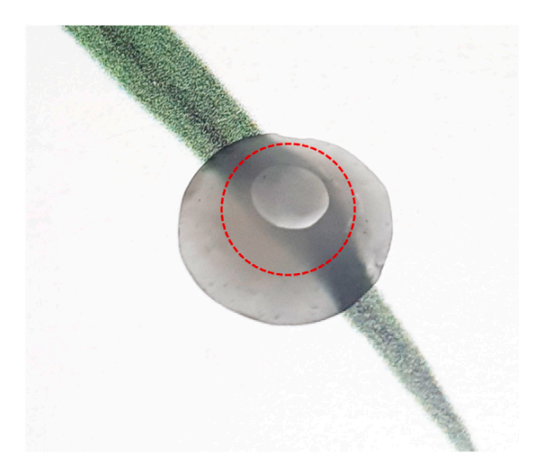


Fig. 4. Cone specimen prepared for the transparency measurements. Red circle highlights the polished surface prepared for the measurements. (For interpretation of the references to colour in this figure legend, the reader is referred to the Web version of this article.)

mechanical (stress-strain), densification, and grain growth components involved during the SPS. The model's framework and boundary conditions are described below.

The model incorporates the following five components: a) electrical current's flow, b) Joule heating, c) mechanical deformation, d) densification (sintering model and cold compaction), and e) grain growth. The first two involve the graphite tooling, foil, and porous interface, considering the different conductivity at their contacts. Moreover, the porosity evolution in the porous assembly has been considered to evaluate its influence on the thermal and electrical conductivity.

The last three components are considered for the porous assembly (sintering part and porous interface).

 a) Electrical Current Flow: The conservation of electrical current is defined as:

$$\nabla \bullet \vec{J} = 0 \tag{1}$$

where the current density \vec{J} [A m⁻²] is related to the electric field \vec{E} [V m⁻¹] though the electrical conductivity λ [S m⁻¹] ($\vec{J} = \lambda \vec{E}$). Considering a static problem where $\nabla \times \vec{E} = 0$, the electric field can be defined in terms of electrostatic potential V [V] ($\vec{E} = -\nabla V$). The combination of these relationships results in a second-order partial differential equation:

$$\nabla \bullet \vec{J} = \nabla \bullet \left(\lambda \vec{E} \right) = \nabla \bullet |\lambda(-\nabla V)| = -\nabla \bullet (\lambda \nabla V) = 0$$
 (2)

b) Joule Heating and Heat Transfer: defining the energy conservation as:

$$\rho C_P \frac{\partial T}{\partial t} + \nabla \bullet \vec{q} = h \tag{3}$$

presents the time dependence of the temperature in terms of heat flux \vec{q} [W m⁻²] and heat generated h [W m⁻³] ($h = \vec{J} \bullet \vec{E}$) by the electric current density in the material. In Eq. (3) other parameters are present, such as density (ρ) [kg m⁻³] and heat capacity (C_P) [J K⁻¹]. The heat flux vector is defined as $\vec{q} = -k_T \nabla T$, where k_T [W m⁻¹·K] is the thermal conductivity of the material.

All these relationships lead to the second-order partial differential equation:

$$\rho C_{P} \frac{\partial T}{\partial t} + \nabla \bullet \vec{q} = \rho C_{P} \frac{\partial T}{\partial t} + \nabla \bullet (-k_{T} \nabla T) = \rho C_{P} \frac{\partial T}{\partial t} - \nabla \bullet (k_{T} \nabla T) = \left| \vec{J} \right| \left| \vec{E} \right|$$
(4

Coupling the relationship for the conductive media DC described in Eq. (2) and the heat transfer by conduction defined in Eq. (3) allows defining the induced Joule heating as:

$$\begin{cases}
\nabla \bullet (\lambda \nabla V) = 0 \\
\rho C_P \frac{\partial T}{\partial t} - \nabla \bullet (k_T \nabla T) = \lambda |\nabla V|^2
\end{cases}$$
(5)

To take into account the effect of porosity on the temperature-dependent electrothermal properties used in the model the following relationships based on the effective medium approximation [53,54] are utilized:

$$\lambda_{porous} = \lambda(T) \bullet \left(1 - \frac{3}{2}\theta \right) \tag{6}$$

$$k_{T \ porous} = k_{T}(T) \bullet \left(1 - \frac{3}{2}\theta\right)$$
 (7)

$$\rho_{\text{porous}} = \rho(T) \bullet (1 - \theta) \tag{8}$$

$$C_{P \text{ norms}} = C_P(T) \bullet (1 - \theta) \tag{9}$$

In Table 1 the electrothermal materials' properties used for Equations (1)–(9) are reported.

Since the sacrificial interface is surrounded by alumina powder, which has low electrical conductivity, the conductivity value for boron nitride is considered to be only a function of temperature (10[-0.012T+23]) [55]. This assumption has been used due to the challenge represented by determining the influence of the boron nitride layer applied on the porous graphite interface on the electro-resistivity and the respective negligible error that should not affect the calculation results.

 c) Sintering Model: The main constitutive equation for the sintering of a nonlinear viscous porous material can be defined as [59]:

$$\sigma_{ij} = \frac{\sigma_{lc}(W)}{W} \left[\varphi \dot{\varepsilon}_{ij} + \left(\psi - \frac{1}{3} \varphi \right) \dot{e} \delta_{ij} \right] + P_L \delta_{ij}$$
(10)

where σ_{ij} [MPa] represent the externally applied stresses, $\sigma_{lc}(W)$ the effective stress [MPa], W [s^{-1}] the equivalent strain rate, \dot{e} [s^{-1}] the shrinkage rate, \dot{e}_{ij} the strain rate components [s^{-1}], and δ_{ij} the Kronecker's delta. The normalized shear and bulk viscosity moduli φ and ψ , respectively, and the effective sintering stress P_L [MPa] can be written as functions of porosity θ :

Table 1 Electrothermal parameters used in Eqs. (1) - 9)

Parameter	Material	Expression
$\lambda(T)$ [S m ⁻¹]	Electrode Graphite Alumina	$ \begin{array}{l} 1/[(50.2+0.0838.T-1.76\times10^{-5}.T^2)\cdot1\times10^{-8}] \\ 1/[(1.70\times10^{-5}-1.87\times10^{-8})\cdot T+(1.26\times10^{-11})\cdot \\ T^2-(2.46\times10^{-15})\cdot T^3] \\ 1/[(8.7\times10^{19})\cdot T^{-4.82}] \end{array} $
$ \begin{array}{c} C_p(T) \text{ [J kg}^{-1} \\ K^{-1} \end{array}] $	Electrode Graphite Alumina	$\begin{array}{c} 446.5 + 0.162 \text{-T} \\ 34.3 + 2.72 \cdot \text{T} - (9.6 \times 10^{-4}) \cdot \text{T}^2 \\ 850 \end{array}$
$ \begin{array}{c} K_T(T) [Wm^{-1}] \\ K^{-1}] \end{array} $	Electrode Graphite Alumina	$\begin{array}{l} 9.99 + 0.0175 \cdot T \\ 123 - (6.99 \times 10^{-2}) \cdot T + (1.55 \times 10^{-5}) \cdot T^2 \\ 39,500 \cdot T^{-1.26} \end{array}$
ρ(T) [kg m ⁻³]	Electrode Graphite Alumina	7900 1904 – 0.0141·T 3899

$$\varphi = (1 - \theta)^2 \tag{11}$$

$$\psi = \frac{2}{3} \frac{(1 - \theta)^3}{\theta} \tag{12}$$

$$P_L = \frac{3\alpha}{r_0} (1 - \theta)^2 \tag{13}$$

where α [J m $^{-2}$] is the surface energy of the material, and r_o [m] is the average particle size.

The effective stress and the equivalent strain rate for the case of power law creep case can be defined by the following equations:

$$\sigma_{lc}(W) = AW^{m_{lc}} \tag{14}$$

$$W = \frac{1}{\sqrt{1-\theta}} \sqrt{\varphi \dot{\gamma}^2 + \psi \dot{e}^2} \tag{15}$$

where A and m_{lc} are material constants, and $\dot{\gamma}$ [s^{-1}] corresponds to the shape change rate. In a three-dimensional Cartesian coordinate system (x-y-z), the shrinkage and shape rate change correspond to:

$$\dot{e} = \dot{\varepsilon}_{x} + \dot{\varepsilon}_{y} + \dot{\varepsilon}_{z} \tag{16}$$

$$\dot{\gamma} = \sqrt{2\left(\dot{\varepsilon}_{xy}^{2} + \dot{\varepsilon}_{xz}^{2} + \dot{\varepsilon}_{yz}^{2}\right) + \frac{2}{3}\left(\dot{\varepsilon}_{x}^{2} + \dot{\varepsilon}_{y}^{2} + \dot{\varepsilon}_{z}^{2}\right) - \frac{2}{3}\left(\dot{\varepsilon}_{x}\dot{\varepsilon}_{y} + \dot{\varepsilon}_{x}\dot{\varepsilon}_{z} + \dot{\varepsilon}_{y}\dot{\varepsilon}_{z}\right)}$$
(17)

The temperature dependence of the pre-exponential factor in Eq. (10) can be defined through Arrhenius equation:

$$A = A_0 T^{m_{lc}} \exp\left(\frac{m_{lc} Q_{lc}}{RT}\right) \tag{18}$$

where A_0 is a power law creep factor, T [K] the absolute temperature, R [$J \cdot K^{-1} \cdot mol^{-1}$] the gas constant, and Q_{lc} [J K^{-1} mol^{-1}] the power law creep activation energy.

To determine the value of m_{lc} , A_0 and, Q_{lc} the experimental method described in the work of Manière et al. [45] was followed, the obtained results are shown in Table 2.

The porosity θ determines the general behavior of the porous material. The densification of the material can be determined though the porosity's evolution, which can be defined using the continuity equation:

$$\frac{\dot{\theta}}{1-\theta} = \dot{e} \tag{19}$$

d) Cold Compaction: The porous graphite interface during the SPS process densified due the effect of the compaction, therefore the main constitutive equation (Eq. 10) has to be modified as (assuming a negligible value of the effective sintering stress):

$$\sigma_{ij} = \frac{\sigma_c(W)}{W} \left[\varphi \dot{\varepsilon}_{ij} + \left(\psi - \frac{1}{3} \varphi \right) \dot{e} \delta_{ij} \right]$$
 (20)

Table 2
Parameters used in Eqs.(10) - 24)

$k_0 \left[m^3 s^{-1} \right]$	$1.8 \ 10^{-5}$
θ_{cr} [-] [57]	0.08
$Q_G [J K^{-1} mol^{-1}]$	464,000
$\alpha [J m^{-2}] [58]$	1.12
A_0 [Pa s]	$2.5 \ 10^{-3}$
m_{lc} [-]	1
$Q_{lc} [J K^{-1} mol^{-1}]$	179,000
m_c [-]	0
σ_{Y} [MPa]	60
G_0 [μm]	3.5

The effective stress for the cold compaction process becomes [52, 59]:

$$\sigma_c(W) = \sigma_Y W^{m_c} \tag{21}$$

where σ_Y [MPa] is the yield strength of the material subjected to the compaction and the creep parameter $m_c \sim 0$. To determine the value of σ_Y and m_c , the graphite powder was subjected to multi-step pressure dilatometry [60,61].

e) *Grain Growth*: The temperature dependence of the grains' size can be defined as [30,56]:

$$\frac{dG}{dt} = \frac{k_0}{3G^2} \left(\frac{\theta_{cr}}{\theta + \theta_{cr}}\right)^{\frac{3}{2}} exp\left(-\frac{Q_G}{RT}\right)$$
(22)

where the materials parameters k_0 [m³ s⁻¹] and Q_G [kJ K⁻¹mol⁻¹] are respectively the pre-exponential factor and the activation energy for the grain growth, and θ_{cr} is a critical value which represents the transition from open to closed porosity. The value of the material's parameters k_0 and Q_G were experimentally determined [62], showing values close to those already reported in literature for the grain growth of alumina [63, 64].

The grain growth influence on the behavior of the sintering porous material can be included in Eqs. (13) and (18) and modifies them as follows:

$$P_L = \frac{3\alpha}{G} (1 - \theta)^2 \tag{23}$$

$$A = A_0 T^{m_{lc}} \exp\left(\frac{m_{lc} Q_{lc}}{RT}\right) \left(\frac{G}{G_0}\right)^2 \tag{24}$$

where G_0 [µm] is the initial average grain size.

The material parameters used in the model for the alumina powder, which composes the sintered transparent cone, and the graphite, which composes the porous interface, are present in Table 2.

4. Results and discussion

Additive manufacturing technologies, such as binder jetting and solvent jetting, allow the production of sacrificial porous interfaces which enable the manufacturing of complex shaped components with homogeneous microstructure. The developed SPS model embedded in the finite element software COMSOL® was used to simulate the sintering behavior of the porous assembly and the results were compared with the corresponding experiments. The experimental results allowed the validation of the model's capability to predict the sintering process outcome and the methodology of manufacturing transparent complex shaped components through the combination of additive manufacturing and spark plasma sintering. In the sections below the results of the characterization of the conical transparent parts and the electro-thermomechanical model for the SPS are shown and compared.

4.1. Transmittance of complex shape sample

The manufactured cone shown in Fig. 4 is transparent enough to allow to observe the image directly beneath the sample. To quantify the transparency of the sintered specimens through the in-line transmittance measurements the tip of the cone has been removed and the obtained flat surface has been carefully prepared to conduct the measurements.

Fig. 5 shows the in-line transmittance measured, where the highest transmittance measured was in the visible light range: 16 % at 490 nm of wavelength.

The obtained measurements can be correlated with the microstructure observed in the part (described in the next section) and can also be affected by the sample's geometry and thickness. In other works [65]

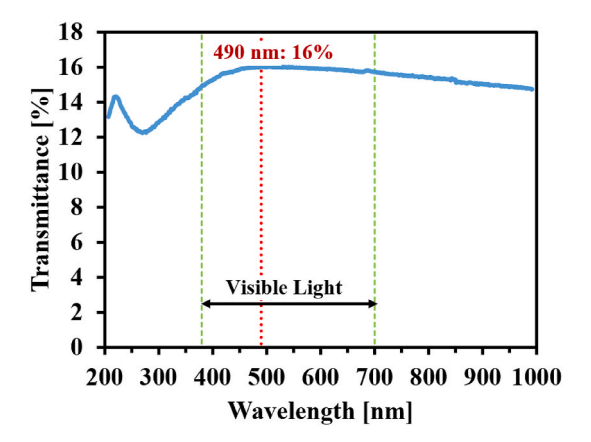


Fig. 5. In-line transmittance measurements, the green area represents the visible light range, the red arrow shows the highest value of transmittance. (For interpretation of the references to colour in this figure legend, the reader is referred to the Web version of this article.)

have been shown how either the geometry and the dimension of the specimens can induce some disturbance of the passing light used to conduct the in-line transmittance measurements resulting in values slightly smaller from those previously obtained from simple shaped specimens [57].

4.2. Microstructure and mechanical properties

The transparent complex-shaped parts show a density of $3.90~\rm g~cm^{-3}$, which corresponds to $98.7~\rm \%$ of relative density. This achieved high density together with a uniform microstructure, as demonstrated by the measurements of grain size and microhardness, which are shown below, is fundamental for the transparency, since the presence of pores induces the light diffraction phenomenon [66,67]. The microstructure observation, grain size, and hardness measurements were conducted on different areas of the samples (Fig. 6); the locations analyzed are indicated as A close to the top surface, B close to the bottom surface, C in the center of the cross-section.

The value of the transparency measured can be explained by observing the microstructure (Fig. 6). The thermal etching allowed to highlight the grain boundary and, consequently, to measure the grain size obtained at the end of the SPS process in the different specimen regions: top surface (A), bottom surface (B) and, in the core (C).

The microstructure obtained is homogeneous in the different regions as can be noticed in the micrograph reported in Fig. 6. The collected images were analyzed using the image analysis software ImageJ® following the planimetric procedure described by ASTM E112-13 [68] to

calculate the grain size in all the observed areas. The average grain size measured is: $6.96\pm0.65~\mu m$ at A, $7.28\pm0.63~\mu m$ in the region B, and $6.90\pm0.54~\mu m$ in the region C, confirming the qualitative analysis and showing how the microstructure obtained is homogeneous. Also, the residual porosity is homogeneously distributed, an important factor in obtaining a transparent component [65]. Hardness is another parameter that can be used to evaluate the homogeneity of the microstructure in terms of grain size since these two material parameters are correlated by the Hall-Petch relationship [69,70].

In Fig. 7 the hardness measurements of the different regions of the transparent Al_2O_3 samples are shown, and the homogeneity of the microstructure can be noticed by looking at the obtained values: the highest hardness value was measured at the bottom surface (1862 \pm 245 HV) and the lowest at the top surface (1634 \pm 311 HV).

The hardness values are in agreement with similar values obtained in a previous work [57] for the same alumina grain size measured at the different areas.

A homogeneous microstructure with a grain size below a certain dimension is very important for transparency since a larger grain size leads to stronger scattering [60,71].

4.3. Model

The model described in section 3, which had as input the process parameters utilized in the real experiments, was employed to run simulation which allowed obtaining from the current pathway (Fig. 8 (a)) the current density distribution in the tooling during the sintering process (Fig. 8(b)), which renders the corresponding thermal distribution (Fig. 8(c)).

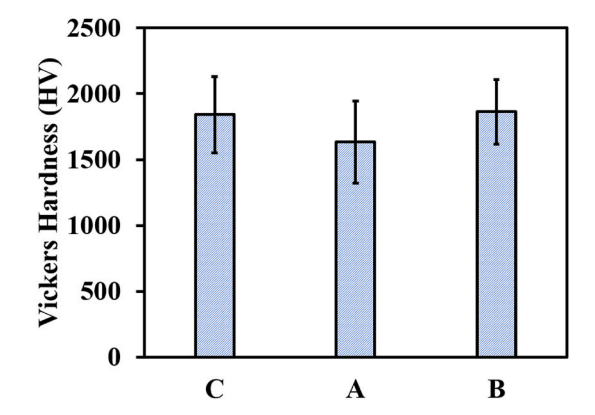


Fig. 7. Hardness values measured at the different locations: (A) top surfaces, (B) bottom surfaces and (C) center.

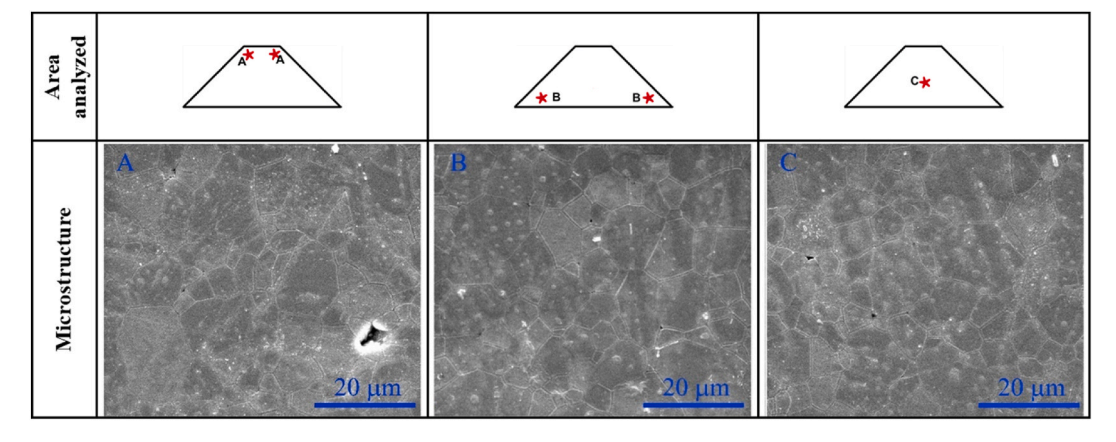


Fig. 6. Location of the different areas where the microstructure observations, measurements of grain size and hardness were conducted and the respective microstructures.

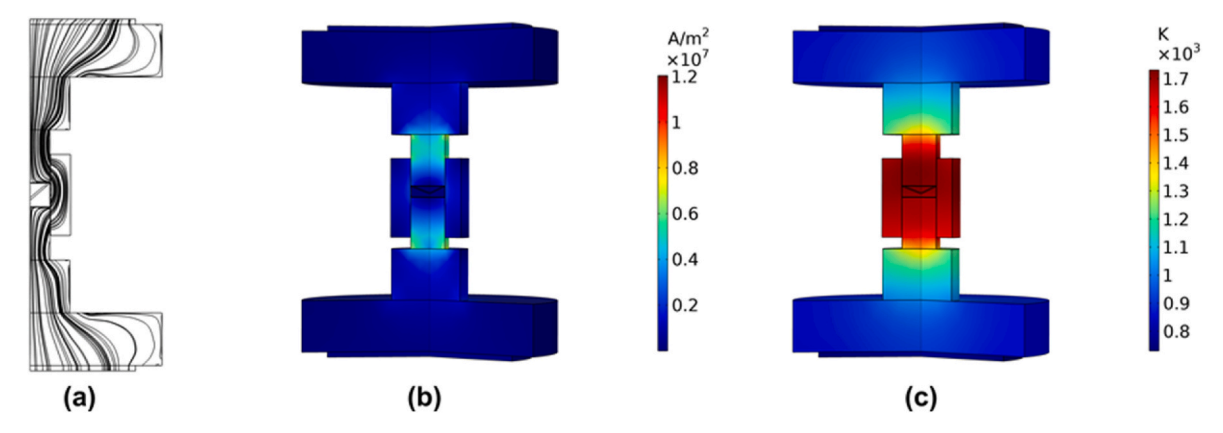


Fig. 8. FEM model result (a) current lines, (b) electrical current density (A/m^2) , (c) Temperature (K).

It is possible to notice a higher current density distribution in the vicinity of the contacts with the graphite punches where the electric current lines are tighter. Therefore, the electric current density achieved in these areas is greater, and consequently, the higher temperature is generated in the vicinity of the die, where the heat dissipation is limited thanks to the external graphite felt.

The temperature distribution determined by the electro-thermal part of the FEM code allows the mechanical part of the FEM code to determine the density and grain size distribution in the powder component, as shown in Fig. 9 (a),(b),(c).

As possible to notice, the calculated density and grain size distribution are homogeneous in all the component volumes. There are smaller variations of the values only in the proximity of the cone surface, which was in contact with the printed porous graphitic interface (Fig. 9(a)); this can be explained by the continuity of the FEM model's elements since the interface subjected only to cold compaction has lower relative density in the vicinity of the surface of the sintered component.

Moreover, it is possible to notice how the modeling results are in agreement with the average values obtained with the experimental results (Fig. 10).

The model is capable of calculating the average grain size in the different locations, and it can also approximate the relative density, the measured value obtained by the model is 99 %.

The model results enable the optimization of the design of the sacrificial porous interface and the sintering process based on the desired component geometry and microstructure through "virtual" experiments, substantially reducing the experimental campaign needed to determine the optimal process parameters. This result is fundamental in the case of lenses in which the dimension (e.g., curvature, thickness) and the grain structure are fundamental parameters determining the optical properties.

5. Conclusions

The integration of additive manufacturing and spark plasma

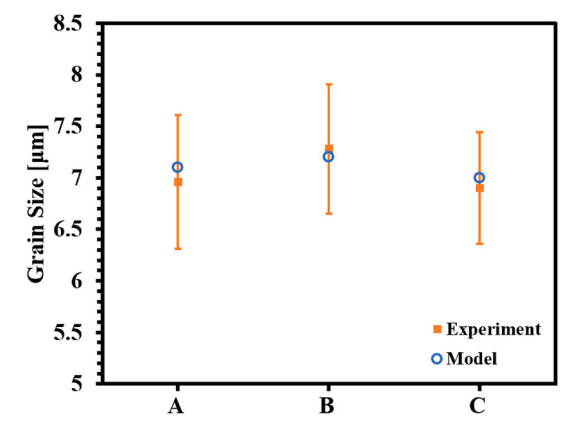


Fig. 10. Grain size FEM model and experiment comparison.

sintering has been successfully utilized to produce complex-shape transparent ceramics. A porous deformable interface that defines the geometry of the component has been produced using a solvent-jetting printer. After the sintering of the porous assembly composed of the interface and the loose ${\rm Al_2O_3}$ powder, the transparent complex shape alumina part has been obtained.

A comprehensive, three-dimensional fully coupled thermo-electromechanical finite element framework has been developed for modeling the SPS process of the porous assembly, which can help in optimization of the complex-shape transparent alumina part. The difficulties arise in the determination of the correct electrical resistance introduced by the presence of the boron nitride layer on the porous interface. Despite the simplification introduced by the assumption of the electroconductivity being only function of temperature and not considering some changes during the sintering process, which could have affected the boron nitride layer, the model has shown its capability to adequately describe the densification and the microstructural

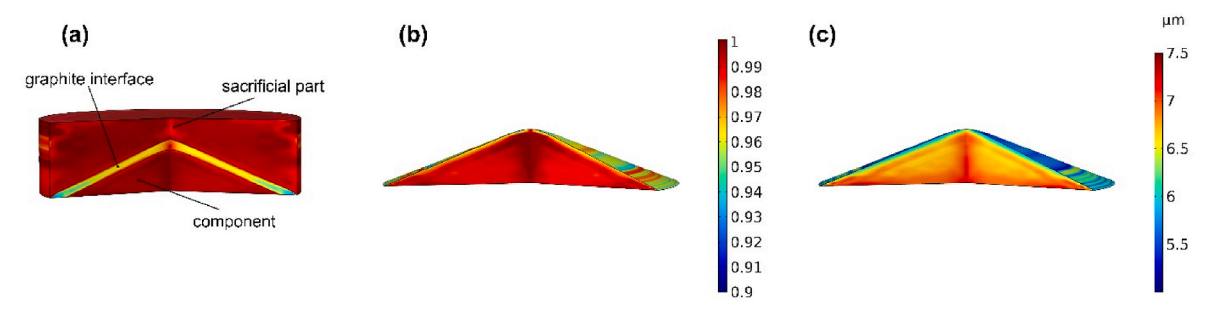


Fig. 9. FEM model result: (a) porous assembly, (b) component relative density and, (c) grain size (μm).

evolution of the alumina component.

CRediT authorship contribution statement

Elisa Torresani: Writing – review & editing, Writing – original draft, Supervision, Funding acquisition, Conceptualization. CheolWoo Park: Methodology, Investigation, Data curation. Thomas Grippi: Writing – original draft, Software, Investigation. Chris Haines: Writing – review & editing. Eugene A. Olevsky: Writing – review & editing, Writing – original draft, Supervision, Funding acquisition, Conceptualization.

Declaration of competing interest

The authors declare that they have no known competing financial interests or personal relationships that could have appeared to influence the work reported in this paper.

Acknowledgements

The support of US Army DEVCOM - Army Research Laboratory (Contract W911–NF-20-2-0226) is gratefully appreciated. The support of the National Science Foundation (Grants 1900876, 2138421, and 2119832) is gratefully acknowledged.

References

- [1] J. Lu, K.I. Ueda, H. Yagi, T. Yanagitani, Y. Akiyama, A.A. Kaminskii, Neodymium doped yttrium aluminum garnet (Y3Al5012) nanocrystalline ceramics—a new generation of solid state laser and optical materials, J. Alloys Compd. 341 (1–2) (2002) 220–225.
- [2] S.D. Zhang, F.X. Sun, X.L. Xia, C. Sun, L.M. Ruan, Multi-layer-combination method to retrieve high-temperature spectral properties of C-plane sapphire, Int. J. Heat Mass Tran. 121 (2018) 1011–1020.
- [3] I. Milisavljevic, Y. Wu, Current status of solid-state single crystal growth, BMC Materials 2 (2020) 1–26.
- [4] A. Ikesue, Y.L. Aung, T. Kamimura, S. Honda, Y. Iwamoto, Composite laser ceramics by advanced bonding technology, Materials 11 (2) (2018) 271.
- [5] W. Liu, J. Li, B. Jiang, D. Zhang, Y. Pan, 44 KW laser output of Nd: YAG ceramic slab fabricated by a solid-state reactive sintering, J. Alloys Compd. 538 (2012) 258–261. 2.
- [6] P. Lecoq, Development of new scintillators for medical applications, Nucl. Instrum. Methods Phys. Res. 809 (2016) 130–139.
- [7] G.C. Wei, Transparent ceramic lamp envelope materials, J. Phys. D 38 (17) (2005) 3057.
- [8] H. Mizuta, K. Oda, Y. Shibasaki, M. Maeda, M. Machida, K. Ohshima, Preparation of high-strength and translucent alumina by hot isostatic pressing, J. Am. Ceram. Soc. 75 (2) (1992) 469–473.
- [9] W. Liu, B. Liu, J. Liu, Y. Pan, J. Guo, Effects of characteristics of Y2O3 commercial powders on structural and optical properties of Nd: YAG ceramics, Ceram. Int. 40 (7) (2014) 11399–11404.
- [10] S.H. Lee, S. Kochawattana, G.L. Messing, J.Q. Dumm, G. Quarles, V. Castillo, Solid-state reactive sintering of transparent polycrystalline Nd: YAG ceramics, J. Am. Ceram. Soc. 89 (6) (2006) 1945–1950.
- [11] J. Petit, P. Dethare, A. Sergent, R. Marino, M.H. Ritti, S. Landais, J.L. Lunel, S. Trombert, Sintering of α-alumina for highly transparent ceramic applications, J. Eur. Ceram. Soc. 31 (11) (2011) 1957–1963.
- [12] M. Trunec, K. Maca, R. Chmelik, Polycrystalline alumina ceramics doped with nanoparticles for increased transparency, J. Eur. Ceram. Soc. 35 (3) (2015) 1001–1009.
- [13] K. Drdlíková, R. Klement, D. Drdlík, T. Spusta, D. Galusek, K. Maca, Luminescent Er3+ doped transparent alumina ceramics, J. Eur. Ceram. Soc. 37 (7) (2017) 2695–2703.
- [14] A.C. Sutorik, G. Gilde, J.J. Swab, C. Cooper, R. Gamble, E. Shanholtz, The production of transparent MgAl2O4 ceramic using calcined powder mixtures of Mg (OH) 2 and γ-Al2O3 or AlOOH, Int. J. Appl. Ceram. Technol. 9 (3) (2012) 575–587.
- [15] A. Krell, J. Klimke, T. Hutzler, Advanced spinel and sub-μm Al2O3 for transparent armour applications, J. Eur. Ceram. Soc. 29 (2) (2009) 275–281.
- [16] K.I. Rybakov, E.A. Olevsky, E.V. Krikun, Microwave sintering: fundamentals and modeling, J. Am. Ceram. Soc. 96 (4) (2013) 1003–1020.
- [17] M. Oghbaei, O. Mirzaee, Microwave versus conventional sintering: a review of fundamentals, advantages and applications, J. Alloys Compd. 494 (1–2) (2010) 175–189
- [18] V.V. Yakovlev, S.M. Allan, M.L. Fall, H.S. Shulman, Computational study of thermal runaway in microwave processing of zirconia. Microwave and RF Power Applications, 2011, pp. 303–306.
- [19] J. Croquesel, D. Bouvard, J.M. Chaix, C.P. Carry, S. Saunier, Development of an instrumented and automated single mode cavity for ceramic microwave sintering: application to an alpha pure alumina powder, Mater. Des. 88 (2015) 98–105.

- [20] R. Wroe, A.T. Rowley, Evidence for a non-thermal microwave effect in the sintering of partially stabilized zirconia, J. Mater. Sci. 31 (1996) 2019–2026.
- [21] F. Zuo, S. Saunier, C. Meunier, D. Goeuriot, Non-thermal effect on densification kinetics during microwave sintering of α-alumina, Scripta Mater. 69 (4) (2013) 331–333
- [22] K.I. Rybakov, E.A. Olevsky, V.E. Semenov, The microwave ponderomotive effect on ceramic sintering, Scripta Mater. 66 (12) (2012) 1049–1052.
- [23] E.A. Olevsky, A.L. Maximenko, E.G. Grigoryev, Ponderomotive effects during contact formation in microwave sintering, Model. Simulat. Mater. Sci. Eng. 21 (5) (2013) 055022.
- [24] J. Cheng, D. Agrawal, Y. Zhang, R. Roy, Microwave reactive sintering to fully transparent aluminum oxynitride (ALON) ceramics, J. Mater. Sci. Lett. 20 (1) (2001) 77–79.
- [25] J. Cheng, D. Agrawal, Y. Zhang, R. Roy, Microwave sintering of transparent alumina, Mater. Lett. 56 (4) (2002) 587–592.
- [26] L. Esposito, A. Piancastelli, Y. Bykov, S. Egorov, A. Eremeev, Microwave sintering of Yb: YAG transparent laser ceramics, Opt. Mater. 35 (4) (2013) 761–765.
- [27] Y. Han, J. Feng, J. Zhou, F. Li, X. Huang, L. Wang, G. Liu, J. Cheng, Heating parameter optimization and optical properties of Nd: YAG transparent ceramics prepared by microwave sintering, Ceram. Int. 46 (13) (2020) 20847–20855.
- [28] C. Manière, T. Zahrah, E.A. Olevsky, Inherent heating instability of direct microwave sintering process: sample analysis for porous 3Y-ZrO2, Scripta Mater. 128 (2017) 49–52.
- [29] S. Marinel, E. Savary, M. Gomina, Sintering of CuO and ZnO in a single mode microwave cavity with shrinkage control, JMPEE 44 (1) (2010) 57–63.
- [30] C. Manière, G. Lee, E. Torresani, J.F. Gerling, V.V. Yakovlev, D. Martin, E. A. Olevsky, Flash microwave pressing of zirconia, J. Am. Cer. Society 103 (8) (2020) 4110–4121.
- [31] G. Kerbart, C. Harnois, C. Bilot, S. Marinel, Pressure-assisted microwave sintering: a rapid process to sinter submicron sized grained MgAl2O4 transparent ceramics, J. Eur. Ceram. Soc. 39 (9) (2019) 2946–2951.
- [32] S.H. Risbud, C.H. Shan, A.K. Mukherjee, M.J. Kim, J.S. Bow, R.A. Holl, Retention of nanostructure in aluminum oxide by very rapid sintering at 1150 C, J. Mater. Res. 10 (2) (1995) 237–239.
- [33] L.A. Stanciu, V.Y. Kodash, J.R. Groza, Effects of heating rate on densification and grain growth during field-assisted sintering of a-Al2O3 and MoSi2 powders, Metall. Mater. Trans. A 32 (10) (2001) 2633–2638.
- [34] Z. Shen, M. Johnsson, Z. Zhao, M. Nygren, Spark plasma sintering of alumina, J. Am. Ceram. Soc. 85 (8) (2020) 1921–1927.
- [35] Y. Zhou, K. Hirao, Y. Yamauchi, S. Kanzaki, Densification and grain growth in pulse electric current sintering of alumina, J. Eur. Ceram. Soc. 24 (12) (2004) 3465–3470.
- [36] Y. Shan, X. Wei, X. Sun, J. Xu, Q. Qin, E.A. Olevsky, Highly infrared transparent spark plasma sintered AlON ceramics, J. Mater. Res. 32 (17) (2017) 3279–3285.
- [37] Y. Shan, X. Wei, X. Sun, E. Torresani, E.A. Olevsky, J. Xu, Effect of heating rate on properties of transparent aluminum oxynitride sintered by spark plasma sintering, J. Am. Ceram. Soc. 102 (2) (2019) 662–673.
- [38] B.N. Kim, K. Hiraga, K. Morita, H. Yoshida, Effects of heating rate on microstructure and transparency of spark-plasma-sintered alumina, J. Eur. Ceram. Soc. 29 (2) (2009) 323–327.
- [39] S. Grasso, B.N. Kim, C. Hu, G. Maizza, Y. Sakka, Highly transparent pure alumina fabricated by high-pressure spark plasma sintering, J. Am. Ceram. Soc. 93 (9) (2010) 2460–2462.
- [40] S. Grasso, C. Hu, G. Maizza, B.N. Kim, Y. Sakka, Effects of pressure application method on transparency of spark plasma sintered alumina, J. Am. Ceram. Soc. 94 (5) (2011) 1405–1409.
- [41] Ratzker, B., Wagner, A., Sokol, M., Kalabukhov, S., Dariel, M.P. and Frage, N., Optical and mechanical properties of transparent alumina fabricated by highpressure spark plasma sintering. J. Eur. Ceram. Soc., 39(8), (219), 2712-2719.
- [42] B.N. Kim, K. Hiraga, S. Grasso, K. Morita, H. Yoshida, H. Zhang, Y. Sakka, High-pressure spark plasma sintering of MgO-doped transparent alumina, J. Ceram. Soc. Jpn. 120 (1399) (2012) 116–118.
- [43] M. Stuer, Z. Zhao, U. Aschauer, P. Bowen, Transparent polycrystalline alumina using spark plasma sintering: effect of Mg, Y and La doping, J. Eur. Ceram. Soc. 30 (6) (2010) 1335–1343.
- [44] S. Ghanizadeh, S. Grasso, P. Ramanujam, B. Vaidhyanathan, J. Binner, P. Brown, J. Goldwasser, Improved transparency and hardness in α-alumina ceramics fabricated by high-pressure SPS of nanopowders, Ceram. Int. 43 (1) (2017) 275–281.
- [45] C. Manière, L. Durand, A. Weibel, C. Estournès, Spark-plasma-sintering and finite element method: from the identification of the sintering parameters of a submicronic α-alumina powder to the development of complex shapes, Acta Mater. 102 (2016) 169–175.
- [46] K. Matsugi, H. Kuramoto, O. Yanagisawa, M. Kiritani, A case study for production of perfectly sintered complex compacts in rapid consolidation by spark sintering, Mater. Sci. Eng. 354 (1–2) (2003) 234–242.
- [47] H. Kim, O. Gillia, P. Dorémus, D. Bouvard, Near net shape processing of a sintered alumina component: adjustment of pressing parameters through finite element simulation, Int. J. Mech. Sci. 44 (12) (2002) 2523–2539.
- [48] C. Manière, L. Durand, A. Weibel, G. Chevallier, C. Estournès, A sacrificial material approach for spark plasma sintering of complex shapes, Scripta Mater. 124 (2016) 126–128.
- [49] C. Manière, E. Nigito, L. Durand, A. Weibel, Y. Beynet, C. Estournes, Spark plasma sintering and complex shapes: the deformed interfaces approach, Powder Technol. 320 (2017) 340–345.

- [50] C. Manière, E. Torresani, E.A. Olevsky, Simultaneous spark plasma sintering of multiple complex shapes, Materials 12 (4) (2019) 557.
- [51] C. Manière, G. Lee, E.A. Olevsky, Flash sintering of complex shapes, Appl. Mater. Today 26 (2022) 101293.
- [52] E. Torresani, M. Carrillo, C. Haines, D. Martin, E. Olevsky, Fabrication of powder components with internal channels by spark plasma sintering and additive manufacturing, J. Eur. Ceram. Soc. 43 (3) (2023) 1117–1126.
- [53] R. Orru, R. Licheri, A.M. Locci, A. Cincotti, G. Cao, Consolidation/synthesis of materials by electric current activated/assisted sintering, Mater. Sci. Eng. R Rep. 63 (4–6) (2009) 127–287.
- [54] K.I. Rybakov, E.A. Olevsky, E.V. Krikun, Microwave sintering: fundamentals and modeling, J. Am. Ceram. 96 (4) (2013) 1003–1020.
- [55] L.G. Carpenter, P.J. Kirby, The electrical resistivity of boron nitride over the temperature range 700 degrees C to 1400 degrees C, J. Phys. Appl. Phys. 15 (7) (1982) 1143.
- [56] E.A. Olevsky, C. Garcia-Cardona, W.L. Bradbury, C.D. Haines, D.G. Martin, D. Kapoor, Fundamental aspects of spark plasma sintering: II. Finite element analysis of scalability, J. Am. Ceram. Soc. 95 (8) (2012) 2414–2422.
- [57] C. Park, E. Torresani, C. Haines, D. Martin, E.A. Olevsky, Transparent Al2O3 fabricated by energy efficient spark plasma sintering, J. Mater. Sci. (2023) 1–14, https://doi.org/10.1007/s10853-023-08768-x.
- [58] R.M. German, Sintering Theory and Practice, John Wiley & Sons INC, New York, 1996, p. 256.
- [59] E.A. Olevsky, Theory of sintering: from discrete to continuum, Mater. Sci. Eng. R Rep. 23 (2) (1998) 41–100.
- [60] W. Li, E.A. Olevsky, J. McKittrick, A.L. Maximenko, R.M. German, Densification mechanisms of spark plasma sintering: multi-step pressure dilatometry, J. Mater. Sci. 47 (2012) 7036–7046.
- [61] G. Lee, M.S. Yurlova, D. Giuntini, E.G. Grigoryev, O.L. Khasanov, J. McKittrick, E. A. Olevsky, Densification of zirconium nitride by spark plasma sintering and high

- voltage electric discharge consolidation: a comparative analysis, Ceram. Int. 41 (10) (2015) 14973–14987.
- [62] C. Manière, T. Grippi, S. Marinel, Estimate microstructure development from sintering shrinkage: a kinetic field approach, Mater. Today Commun. 31 (2022) 103369
- [63] E.A. Olevsky, C. Garcia-Cardona, W.L. Bradbury, C.D. Haines, D.G. Martin, D. Kapoor, Fundamental aspects of spark plasma sintering: II. Finite element analysis of scalability, J. Am. Ceram. Soc. 95 (8) (2012) 2414–2422.
- [64] Y.S. Kwon, G. Son, J. Suh, K.T. Kim, Densification and grain growth of porous alumina compacts, J. Am. Ceram. Soc. 77 (12) (1994) 3137–3141.
- [65] A. Krell, T. Hutzler, J. Klimke, Transmission physics and consequences for materials selection, manufacturing, and applications, J. Eur. Ceram. Soc. 29 (2) (2009) 207–221.
- [66] S.F. Wang, J. Zhang, D.W. Luo, F. Gu, D.Y. Tang, Z.L. Dong, G.E. Tan, W.X. Que, T. S. Zhang, S. Li, L.B. Kong, Transparent ceramics: processing, materials and applications, Prog. Solid State Chem. 41 (1–2) (2013) 20–54.
- [67] R. Boulesteix, A. Maître, L. Chrétien, Y. Rabinovitch, C. Sallé, Microstructural evolution during vacuum sintering of yttrium aluminum garnet transparent ceramics: toward the origin of residual porosity affecting the transparency, J. Am. Ceram. Soc. 96 (6) (2013) 1724–1731.
- [68] ASTM E112-13 Standard Test Methods for Determining Average Grain Size, ASTM Int, West Conshohocken, PA, 2013.
- [69] N.J. Petch, The cleavage strength of polycrystals, J. Iron Steel Inst. 174 (1953) 25–28.
- [70] E.O. Hall, The deformation and ageing of mild steel: III discussion of results, Proc. Phys. Soc. B 64 (9) (1951) 747.
- [71] S. Hříbalová, W. Pabst, Transmittance predictions for transparent alumina ceramics based on the complete grain size distribution or a single mean grain size replacing the whole distribution, J. Eur. Ceram. Soc. 42 (12) (2022) 5093–5107.